

Synthetic aperture metalens

FENG ZHAO,^{1,2} ZICHENG SHEN,² DECHENG WANG,¹ BIJIE XU,¹ XIANGNING CHEN,^{1,3} AND YUANMU YANG^{2,4} 

¹School of Space Information, Space Engineering University, Beijing 101416, China

²State Key Laboratory of Precision Measurement Technology and Instruments, Department of Precision Instrument, Tsinghua University, Beijing 100084, China

³e-mail: xn_chen_edu@163.com

⁴e-mail: ymyang@tsinghua.edu.cn

Received 13 August 2021; revised 8 October 2021; accepted 18 October 2021; posted 19 October 2021 (Doc. ID 440185); published 15 November 2021

Metalenses are ultrathin optical elements that can focus light using densely arranged subwavelength structures. Due to their minimal form factor, they have been considered promising for imaging applications that require extreme system size, weight, and power, such as in consumer electronics and remote sensing. However, as a major impediment prohibiting the wide adoption of the metalens technology, the aperture size, and consequently the imaging resolution, of a metalens are often limited by lithography processes that are not scalable. Here, we propose to adopt a synthetic aperture approach to alleviate the issue, and experimentally demonstrate that, assisted by computational reconstruction, a synthetic aperture metalens composed of multiple metalenses with relatively small aperture size can achieve an imaging resolution comparable to a conventional lens with an equivalent large aperture. We validate the concept via an outdoor imaging experiment performed with a synthetic aperture metalens-integrated near-infrared camera using natural sunlight for target illumination. © 2021 Chinese Laser Press

<https://doi.org/10.1364/PRJ.440185>

1. INTRODUCTION

While conventional refractive optical components are typically bulky and heavy, the demand for compact, lightweight optical components is growing rapidly for various applications ranging from consumer electronics to remote sensing based on unmanned aerial vehicles or satellites [1,2]. In recent years, metasurfaces have emerged as a novel platform for wavefront control [3–11]. Composed of an array of subwavelength-spaced dielectric or metallic antennas with thickness less than or on the order of the wavelength of light, metasurfaces can accurately adjust the phase, amplitude, and polarization of light [12–30], with versatile imaging capability in a compact form factor. Currently, one of the major hurdles for the wide adoption of the metalens technology is its aperture size. Increasing the size of the lens aperture can result in a higher imaging resolution that is critical for both microscopy and long-distance imaging applications. Optical metalenses, with their nanometer-sized, aperiodic feature, are typically fabricated by processes such as electron-beam lithography (EBL) that are costly and time-consuming. Despite the recent adoption of scalable manufacturing techniques such as nanoimprinting and ultraviolet stepper lithography in metalens fabrication [31–34], the preparation of a lithography mask or imprinting mold still cannot be avoided. To date, the largest optical metalens can have an aperture size on the order of a few centimeters [32,35–37]. For certain applications, such as a space telescope, which requires a lens aperture size on the order of meters, the manufacturing of a single metalens of such scale

can be extremely challenging, if not impossible, limited by the current semiconductor fabrication infrastructure.

One way to address the issue of a limited lens aperture size is to synthesize multiple apertures. A synthetic aperture can mix signals from a collection of subapertures to render an image having a resolution comparable to an aperture the size of the circumference of all subapertures [38–42]. It is a technology that has been widely used in the radiofrequency regime. As a landmark example, the Event Horizon Telescope project captured and retrieved the first image of the black hole M87 through aperture synthesis of a global network of radio telescopes [43]. Over the last decades, the synthetic aperture approach has also been adopted in the optical domain for applications ranging from remote sensing to microscopy [44,45].

In this work, we aim to address the aperture size limitation of the optical metalens by adopting the synthetic aperture approach. We show that, by combining multiple metalenses with relatively small aperture size, the maximum cutoff frequency (MCF) of the modulation transfer function (MTF) of the synthetic aperture metalens can be improved to a level that is comparable to a lens with an equivalent large aperture. We explore multiple metalens subaperture arrangements and experimentally demonstrate that, assisted by computational reconstruction [46–48], the synthetic aperture metalens composed of three or four subapertures can achieve an imaging resolution comparable to a conventional lens with an aperture the size double that of all subapertures combined.

We further build a metalens-integrated near-infrared camera and demonstrate the enhancement of the imaging resolution using a synthetic aperture metalens in an outdoor setting using natural sunlight for target illumination. The synthetic aperture approach may effectively reduce the time required to fabricate a large area metalens using a serial process. In addition, it may open a new avenue for constructing metalenses with an effective aperture size on the meter scale, which can be extremely challenging for a single-aperture metalens design.

2. RESULTS

A. Working Principle of a Synthetic Aperture Metalens

Figure 1 schematically shows the comparison between imaging using a conventional metalens and a synthetic aperture metalens. Here, we first assume the ideal transmission phase profile of a metalens as

$$\phi(x, y) = -\frac{2\pi}{\lambda} \left(\sqrt{x^2 + y^2 + f^2} - f \right), \quad (1)$$

where $\phi(x, y)$ is the spatially dependent transmission phase of the composing optical antenna, $\lambda = 800$ nm is the design wavelength, and $f = 30$ mm is the focal length. Note that a relatively long focal length is desirable for providing a high magnification for objects at a faraway distance.

For a conventional single-aperture metalens, the image can be obtained through the convolution of the target object and the point spread function (PSF) of the metalens [Figs. 1(a) and 1(b)], with a typical MTF shown in Fig. 1(c). On the other hand, if we consider a synthetic aperture metalens with two subapertures along the x direction, each with an aperture size identical to the single aperture and with the transmission phase

profile satisfying Eq. (1), the as-obtained image may be blurry due to the additional sidelobes in the PSF as well as the reduced intermediate frequency response of the system's MTF. However, the MCF of the synthetic aperture is improved to a level comparable to an aperture the size of the circumcircle of both subapertures; thus, the fine feature of the target object is retained in the convoluted signal. Subsequently, a sharper image can be recovered from the as-obtained image using recovery algorithms such as the Wiener filter algorithm and the Richardson–Lucy deconvolution algorithm [49–51], with the image resolution along the x direction comparable to a single lens with an aperture size corresponding to the circumcircle of both subapertures, as shown in Fig. 1(d). In contrast, along the y direction, without aperture synthesis, the image resolution is identical to the subaperture resolution.

B. Synthetic Aperture Metalens Design and Characterization

For an optical synthetic aperture, various aperture arrangements have been proposed, such as the “Golay,” “Y,” and “Annular” type [52]. Different arrangements can result in different aperture fill factors, equivalent aperture size, phase error, and PSF sidelobes. In this work, as a prototype, we demonstrate synthetic aperture metalenses with the three most common types of aperture arrangement based on two, three, and four subapertures, respectively. Figures 2(a)–2(c) show the schematic of the designed synthetic aperture metalenses. Each subaperture has a radius of 1 mm. For the two-subaperture metalens, the radius of the circumcircle is 2.5 mm, with a subaperture center distance of 3 mm. Consequently, the fill factor of the synthetic aperture is 0.32, as defined by the ratio of the total area of each subaperture to the area of the

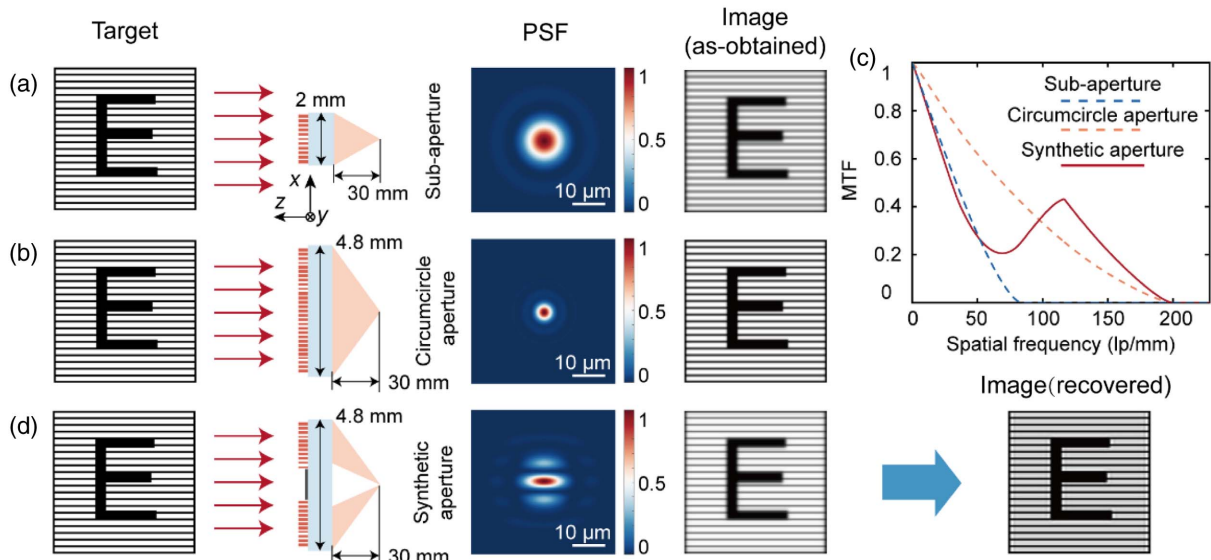


Fig. 1. Imaging principle of a synthetic aperture metalens. (a) Schematic of imaging using a conventional subaperture metalens. The image is obtained through the convolution of the target and the PSF of the metalens. (b) Schematic of imaging using a conventional circumcircle aperture metalens. The image is obtained through the convolution of the target and the PSF of the metalens. (c) Comparison of the MTF of the subaperture metalens (blue dashed line), the circumcircle aperture metalens (orange dashed line), and the synthetic aperture metalens (red solid line); (d) schematic of imaging using a synthetic aperture metalens. The image is first obtained through the convolution of the target and the PSF of the metalens, and then recovered using the Richardson–Lucy deconvolution algorithm. The diameter of the subaperture and the circumcircle aperture is set to 2 and 4.8 mm, respectively.

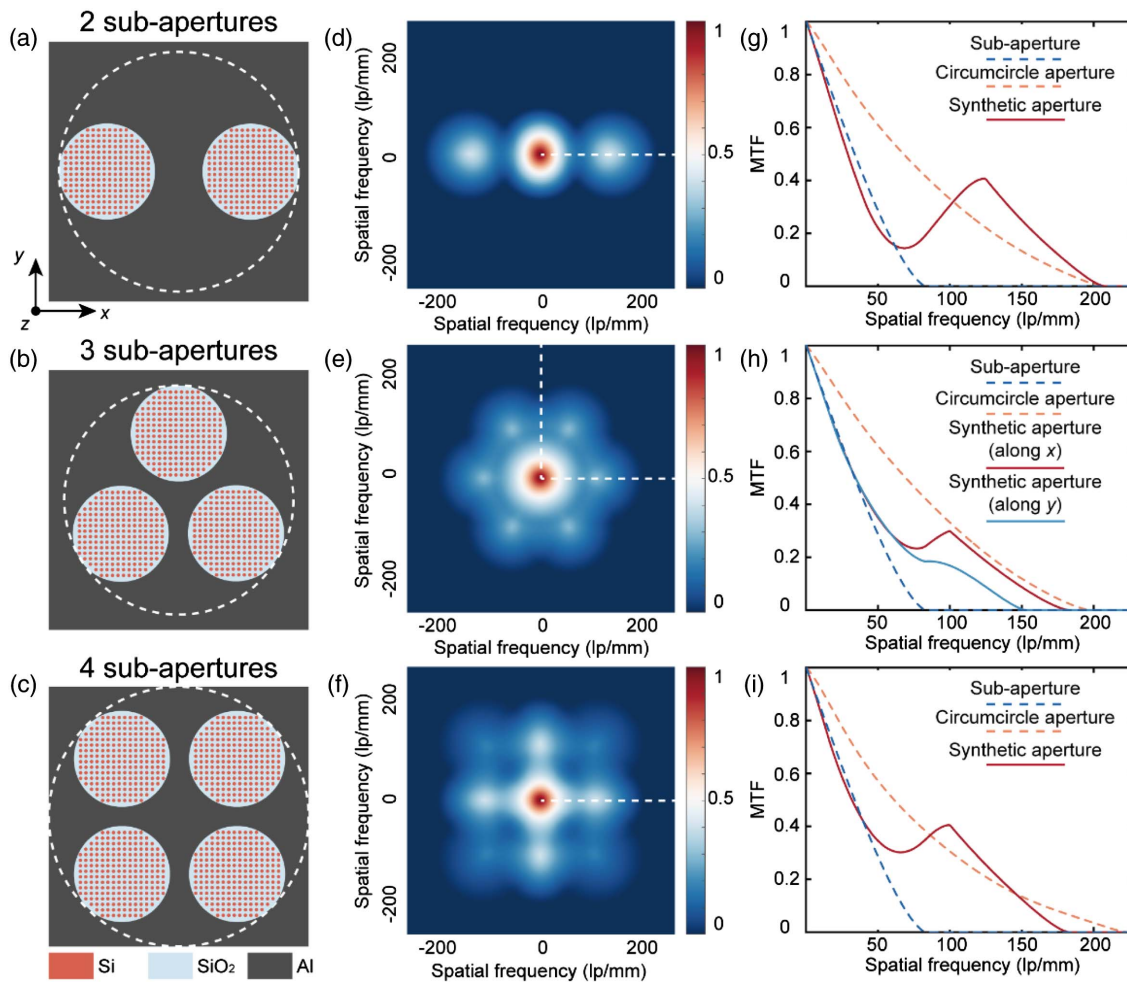


Fig. 2. Arrangement and imaging characteristics of ideal synthetic aperture metalenses. (a)–(c) Schematic of the arrangement of synthetic aperture metalenses with two, three, and four subapertures, respectively. The white dashed line marks the circumcircle of the synthetic aperture. (d)–(f) Calculated MTFs of ideal synthetic aperture metalenses with two, three, and four subapertures, respectively; (g)–(i) MTFs of ideal synthetic aperture metalenses with two, three, and four subapertures, marked by the white dashed line in panels (d)–(f), respectively.

circumcircle [53]. Note that the fill factor effectively determines the reduction of the required time to fabricate the metalens, assuming a serial fabrication process. For the three-subaperture metalens (“Golay-3” type), the connection between the center of each subaperture forms an equilateral triangle. The radius of the circumcircle is 2.38 mm, with the side length of the equilateral triangle of 2.4 mm, corresponding to a fill factor of 0.53. For the four-subaperture metalens, the radius of the circumcircle is 2.7 mm, with a subaperture center distance of 2.4 mm, corresponding to a fill factor of 0.55. We note that although most of the literature has only considered circularly shaped subapertures in a synthetic aperture system, the planar form factor of metalenses may also make it possible to engineer the shape of the subaperture to be noncircular.

With the ideal transmission phase profile of the metalens given in Eq. (1), the MTFs of the subaperture lens, synthetic aperture metalens, and circumcircle aperture lens can be calculated using the angular spectrum method [54], as shown in Figs. 2(d)–2(i). Synthetic aperture metalenses can achieve different MCFs and intermediate frequency characteristics with

varying aperture arrangements. For the two-subaperture design, along the x direction (the direction of synthesis), the MCF of the synthetic aperture metalens is nearly identical to the MCF of the circumcircle aperture lens, with a relatively small intermediate frequency response of less than 0.2. On the other hand, along the y direction, without aperture synthesis, the calculated MCF is close to the MCF of the subaperture lens. For the three-subaperture design with a larger fill factor, the improvement of the MCF can be achieved in both x and y directions, with an intermediate frequency response greater than 0.2. Similarly, the improvement of the MCF is shown in the four-subaperture design, with an intermediate frequency response greater than 0.3.

Figures 3(a)–3(c) show the schematic diagram of the metalens unit cell, an amorphous silicon (a-Si) nanopillar of a height $H = 600$ nm on a 500- μm -thick fused silica (SiO_2) substrate. The a-Si is measured with a refractive index of 3.338 and a negligible absorption at $\lambda_0 = 800$ nm. We simulated the polarization-independent transmission amplitude and phase as a function of the nanopillar radius R for normally incident

light, with a fixed period $U = 400$ nm [Fig. 3(d)], to serve as the library for the metalens design.

The silicon (Si)-based metalenses are fabricated by standard EBL and reactive ion-etching process. 100-nm-thick aluminum was coated around the subapertures to prevent the transmission of background light outside of the lens aperture. The optical images of fabricated synthetic aperture metalenses are shown in Fig. 3(e). A representative scanning electron microscopy (SEM) image of the fabricated sample is shown in Fig. 3(f). The focusing

efficiencies of metalenses with two, three, and four subapertures are experimentally measured and estimated to be 44%, 57%, and 57%, respectively. The relatively low focusing efficiency in the experiment may be due to the size discrepancy of the nano-cylinder as well as defects in the fabricated metalens sample.

The calculated PSFs of the synthetic aperture metalenses of two, three, and four subapertures are shown in Figs. 3(g)–3(i), respectively. To measure the PSF of the synthetic aperture metalens experimentally, we used a collimated laser beam with

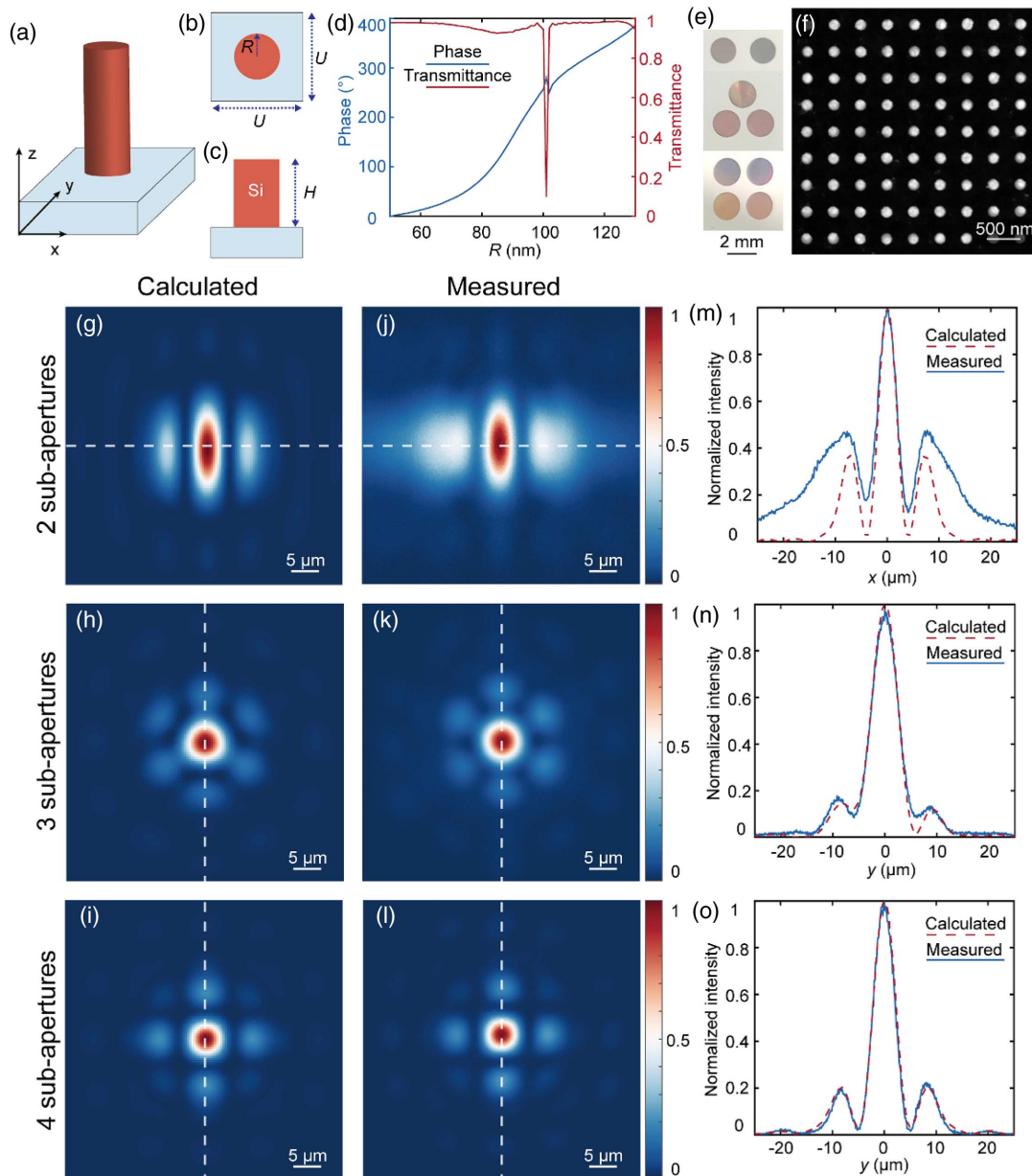


Fig. 3. Design, fabrication, and characterization of the PSF of synthetic aperture metalenses. (a) Schematic of a unit cell of the metalens, consisting of a-Si nanopillars on a glass substrate; (b), (c) top and side views of the Si nanopillar with height H and radius R , located inside a square unit cell with period U ; (d) simulated phase and transmittance of the metalens unit cell as a function of the nanopillar radius; (e) photographs of the fabricated synthetic aperture metalenses with two, three, and four subapertures, respectively; (f) representative top view SEM image of the fabricated metalens sample; (g)–(i) calculated PSFs of ideal synthetic aperture metalenses with two, three, and four subapertures, respectively; (j)–(l) measured PSFs of fabricated synthetic aperture metalenses with two, three, and four subapertures, respectively; (m)–(o) comparison of the calculated and measured PSFs of synthetic aperture metalenses with two, three, and four subapertures, respectively, along the direction specified by the white dashed line in panels (g)–(l).

a central wavelength of 800 nm and a bandwidth of 10 nm as the source. Light impinging from each subaperture is coherently synthesized on the focal plane of the lens, which corresponds to its PSF intensity distribution. The focal plane images, or PSFs, of the metalenses, as shown in Figs. 3(j)–3(l), were captured by a near-infrared camera after image magnification using an objective and a tube lens. Figures 3(m)–3(o) show a comparison of the horizontal cuts of the calculated and measured PSF. For the three- and four-subaperture metalenses, a close agreement between the calculation and measurement is achieved, despite the fact that a relatively large sidelobe in the PSF is measured for the two-subaperture metalens. This is likely due to the fact that the two-subaperture metalens has a lower fill factor and a larger portion of the lens resides toward the edge of the circumcircle of the lens with a large phase gradient, which makes it more susceptible to phase error due to fabrication imperfection.

Subsequently, we used the 1951 United States Air Force (USAF) resolution test chart (Thorlabs Inc.) to compare the resolving power of synthetic aperture metalenses with conventional single-aperture lenses. Figures 4(a)–4(c) show images of the test chart groups 6 and 7 taken using a conventional plano-convex lens (Daheng Optics GCBZ-125L, $f = 30$ mm) with its aperture radius cut to 1, 2.38, and 2.7 mm, respectively, using pinholes that correspond to the radius of the

circumcircle of the synthetic aperture metalenses of two, three, and four subapertures, respectively. In comparison, Figs. 4(d)–4(f) show images directly taken from the synthetic aperture metalenses of two, three, and four subapertures. With the measured PSF of the synthetic aperture metalenses, sharper images are recovered from the relatively blurry as-obtained images from the synthetic aperture metalenses, using the Richardson–Lucy deconvolution algorithm, which is a relatively robust iterative algorithm widely used for recovering a blurred image with a known PSF of the imaging system [55,56]; the recovered images are shown in Figs. 4(g)–4(i). The quality of the recovered image is quantified with the metric of peak signal-to-noise ratio (PSNR) and structural similarity (SSIM) [57], using the image taken by the conventional lens of 2.7-mm-aperture-radius [Fig. 4(c)] as a reference. As is shown in Fig. 4(g), the quality of the image recovered from the two-subaperture metalens is quite poor, likely due to its relatively small fill factor and the rather large sidelobe in its measured PSF. Nevertheless, one can still clearly observe the anisotropy of the image resolution enhancement, with much larger resolution enhancement along the x direction (the direction of aperture synthesis), for the two-subaperture metalens [white dashed box in Fig. 4(g)]. In contrast, the quality of images recovered from both the three-subaperture and

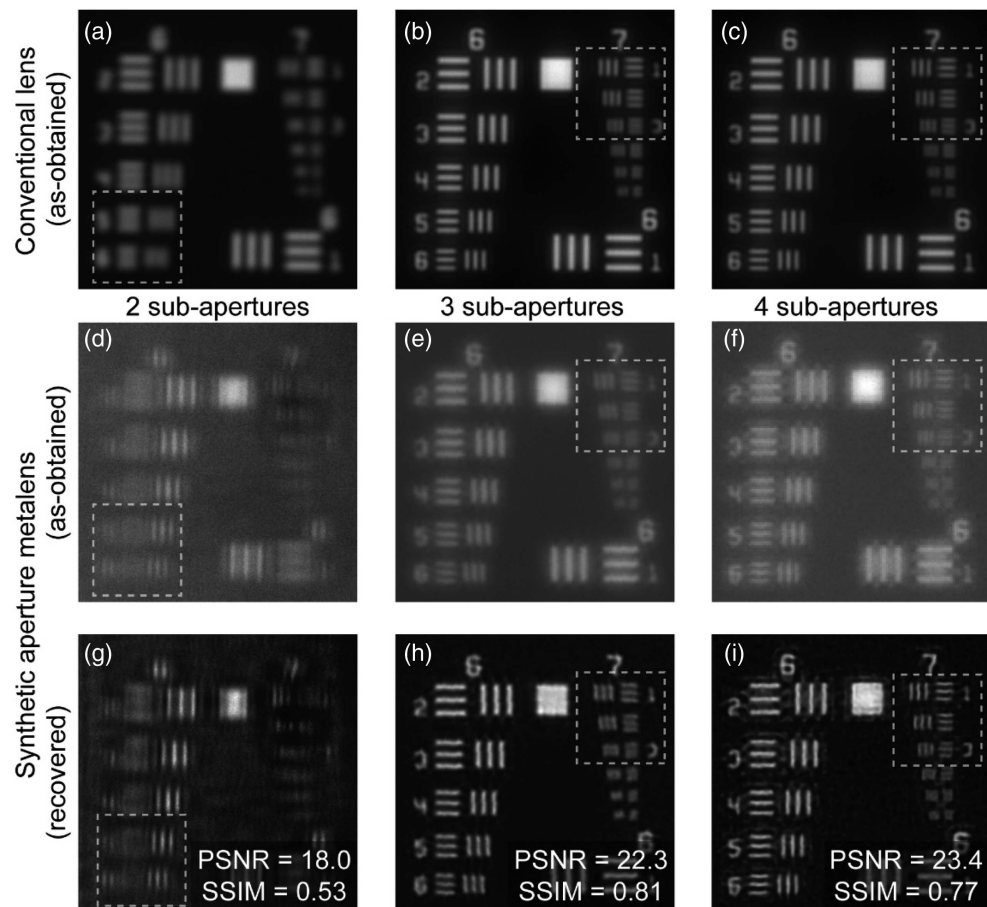


Fig. 4. Characterization of the imaging resolution of synthetic aperture metalenses. (a)–(c) Images of the 1951 United States Air Force (USAF) resolution test chart taken with conventional lenses with an aperture radius of 1, 2.38, and 2.7 mm, respectively; (d)–(f) images of the 1951 USAF resolution test chart directly obtained by synthetic aperture metalenses with two, three, and four subapertures, respectively; (g)–(i) images recovered from the ones directly obtained from synthetic aperture metalenses with the Richardson–Lucy deconvolution algorithm.

four-subaperture metalenses is comparable to the image taken by the conventional lenses with an aperture radius of their circumference. Both the three-subaperture metalens and the corresponding conventional lens can resolve features up to the element 2 of group 7 [white dashed boxes in Figs. 4(b) and 4(h)], while both the four-subaperture metalens and the corresponding conventional lens can resolve features up to the element 3 of group 7 [white dashed boxes in Figs. 4(c) and 4(i)], demonstrating the effectiveness of the synthetic aperture approach to achieve a comparable imaging resolution using about half the aperture size of a single aperture lens. We further notice the PSNR and SSIM value for the four-subaperture metalens are similar to that of the three-subaperture metalens, which is likely due to the larger sidelobe in the PSF and more prominent ghost noise measured for the four-subaperture metalens. In general, ghost noise in the recovered images, as shown in Figs. 4(h) and 4(i), may be further improved by alternative image recovery methods such as Wiener deconvolution or deep learning, although those methods may require a good estimation of the noise power spectrum of the image or prior knowledge of the scene [58–60].

C. Outdoor Imaging Experiment

To further validate the approach, we integrated the synthetic aperture metalens of three subapertures with a near-infrared camera for imaging in the outdoor environment using natural sunlight for illumination. The photograph of the metalens-integrated camera is shown in Fig. 5(a). The distance between the camera sensor and the three-subaperture metalens is set to its focal length to achieve a deep depth of field. We use natural sunlight to illuminate the target (a Tsinghua University logo) placed about 7 m away from the camera. Here, a bandpass filter

with a central wavelength of 800 nm and a bandwidth of 10 nm is inserted before the metalens due to the chromatic aberration of the lens; however, note that the relatively small numerical aperture of the lens may largely simplify the design of an achromatic version of a synthetic aperture metalens [61]. To demonstrate resolution enhancement using the synthetic aperture metalens-integrated camera, two images were first taken with a conventional lens with an aperture radius corresponding to the subaperture and circumference aperture radius of the three-subaperture metalens, as shown in Figs. 5(b) and 5(c), respectively. In comparison, the recovered image from the three-subaperture metalens can resolve the fine lines of the target [black dashed box in Fig. 5(f)], with a resolving power comparable to the conventional circumference-aperture lens [black dashed box in Fig. 5(c)], and greatly improved in comparison with the conventional subaperture lens [black dashed box in Fig. 5(b)]. Note that the gravel-like noise pattern in the background of Fig. 5(f) originates from the image acquisition, not from the image recovery process.

3. DISCUSSION

In summary, we demonstrate that it is an effective approach to synthesize multiple metalenses, each with a relatively small aperture size, to achieve an imaging resolution comparable to a single aperture metalens with a much larger aperture size. Despite that here we present a polarization-independent synthetic aperture metalens working only for a limited wavelength range, one can leverage the rapid development in other sectors of the metalens technology and construct novel multifunctional synthetic aperture metalenses that may be polarization-dependent [23,62], achromatic [61,63–65], or

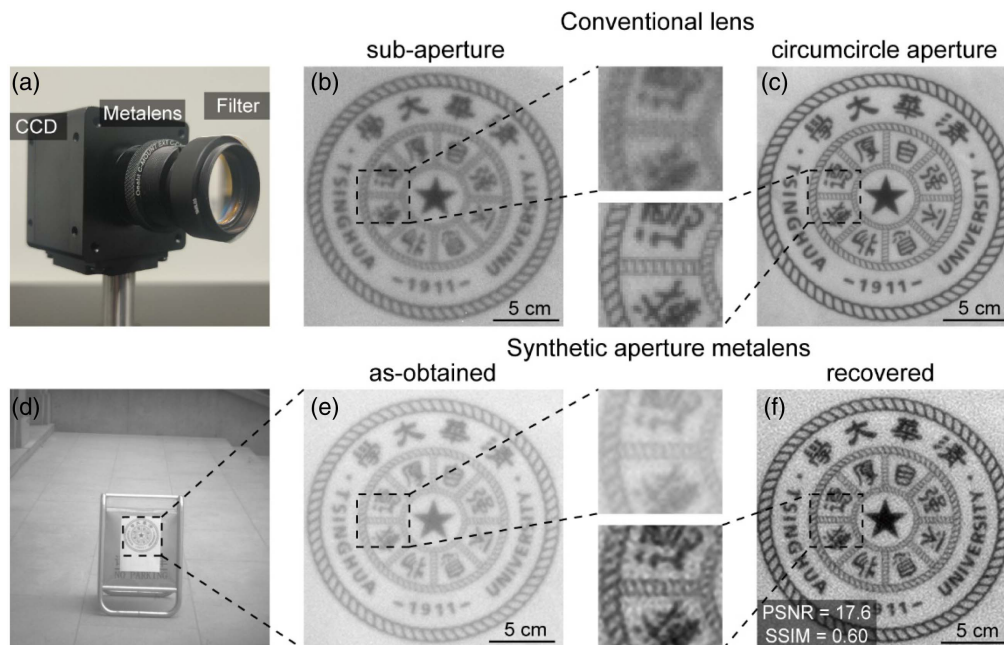


Fig. 5. Outdoor imaging experiment with the metalens-integrated camera. (a) Photograph of the synthetic aperture metalens-integrated near-infrared camera (CCD, charge-coupled device); (b), (c) images directly obtained by conventional lenses with an aperture radius of 1 and 2.38 mm, respectively; (d), (e) images directly obtained by the synthetic aperture metalens with three subapertures; (f) image recovered from the one directly obtained from the synthetic aperture metalens using the Richardson–Lucy deconvolution algorithm.

that can even sense the depth of a scene [26,66,67]. Using flat optical components, a plethora of novel subaperture arrangements that are difficult to realize by bulk lenses due to manufacturing constraints can be envisaged. By combining even more metalenses with a millimeter or centimeter size, it may provide a pathway towards constructing a synthetic aperture metalens with an equivalent aperture size on a much larger scale, thus opening up new avenues for numerous exciting applications ahead.

APPENDIX A: WORKING PRINCIPLE OF A SYNTHETIC APERTURE LENS

The working principle of a synthetic aperture lens has been well established [1,39,53,60]. Here, for the convenience of readers, we reiterate it below. According to the theory of Fourier optics, the imaging process can be described in the spatial domain as

$$g(x, y) = f(x, y) * \text{PSF}(x, y) + n(x, y), \quad (\text{A1})$$

where (x, y) represent the spatial coordinates, $*$ represents a convolution operation, and $f(x, y)$ and $g(x, y)$ are the system input (target object) and system output (acquired image), respectively. $\text{PSF}(x, y)$ is the PSF of the imaging system, and $n(x, y)$ represents the additional noise acquired during the imaging process.

PSF is a metric widely used to quantify the imaging performance of a lens in the spatial domain and can be calculated by the pupil function. For a conventional single-aperture lens with a circular shape, the pupil function can be expressed as

$$P(x, y) = \text{circ}\left(\frac{\sqrt{x^2 + y^2}}{D/2}\right), \quad (\text{A2})$$

where $P(x, y)$ is the pupil function, circ is the circular domain function, and D is the pupil diameter. Subsequently, the PSF of a lens can be obtained by

$$\text{PSF}(x, y) = |\mathcal{F}\{P(x, y)\}|^2, \quad (\text{A3})$$

where \mathcal{F} represents the Fourier transform. The optical transfer function (OTF) of an incoherent imaging system is the normalized form of a Fourier-transformed PSF, which describes the imaging performance of a system in the frequency domain and can be expressed as

$$\text{OTF}(u, v) = \frac{\mathcal{F}\{\text{PSF}(x, y)\}}{\iint \text{PSF}(x, y) dx dy}, \quad (\text{A4})$$

where (u, v) represent the frequency domain coordinates. The MTF is simply the magnitude of the complex OTF.

For a synthetic aperture lens, the pupil is composed of several subapertures with a certain arrangement. In this case, the pupil function of the system shall be rewritten as

$$P_{\text{array}}(x, y) = \sum_{k=1}^N P_{\text{sub}}(x - x_k, y - y_k) e^{i\phi_k(x, y)}, \quad (\text{A5})$$

where $P_{\text{array}}(x, y)$ is the pupil function of the synthetic aperture lens. $P_{\text{sub}}(x, y)$ is the pupil function of each subaperture. N is the number of subapertures. (x_k, y_k) is the central coordinates of the pupil of each subaperture lens. ϕ_k is the phase at which the beam reaches the subaperture. Subsequently, the PSF, OTF, and MTF of a synthetic aperture lens can be calculated according to Eqs. (A3) and (A4).

APPENDIX B: METALENS SIMULATION, FABRICATION, AND FOCUSING EFFICIENCY CHARACTERIZATION

1. Metalens Simulation

The metalens is designed using a-Si nanopillars on top of a fused silica substrate. To achieve the desired transmittance and phase shift, we carried out a geometrical parameter sweep of the nanopillars using the finite-difference time-domain (FDTD) method, with the wavelength of the incident light fixed at 800 nm. The radius (R) of the nanopillar is swept in the range of 100–340 nm while maintaining the height (H) at 600 nm and the period (U) at 400 nm, with a periodic boundary condition.

2. Metalens Fabrication

The fabrication of the synthetic aperture metalens includes the patterning of the a-Si nanopillar-based metalens and the aluminum (Al) mask for blocking the unwanted light transmission outside of the metalens aperture. In the first part, a layer of 600-nm-thick a-Si film is initially deposited onto a fused silica substrate via plasma-enhanced chemical vapor deposition (PECVD). Subsequently, EBL is employed to define the metasurface pattern into the poly(methyl methacrylate) (PMMA) resist. In the following step, the pattern is first transferred to the chromium (Cr) hard mask through lift-off and further transferred to the Si layer via inductively coupled plasma reactive ion etching (ICP-RIE). The Cr mask can then be removed by a wet etchant. The photoresist is spin-coated on the sample. In the second part, the Al mask is precisely patterned outside of

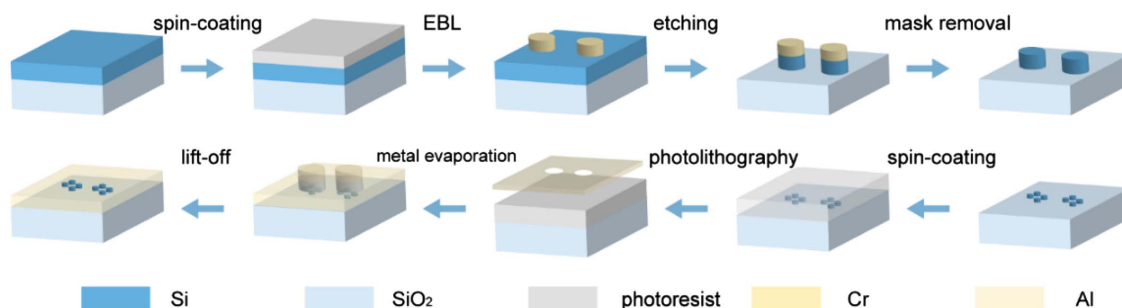


Fig. 6. Schematic of the fabrication process of the synthetic aperture metalens.

the metalens aperture using alignment marks through a serial process of photolithography, electron beam evaporation, and lift-off. A graphical summary of the fabrication process of the synthetic aperture metalens, including the patterning of the Si nanopillar-based metalens and the Al mask for blocking the unwanted light transmission outside of the metalens aperture is shown in Fig. 6.

3. Metalens Efficiency Characterization

To estimate the focusing efficiency of the metalens, we use a supercontinuum laser (YSL SC-PRO-15) coupled with a tunable acoustic-optic bandpass filter as the light source. We then use a photodetector (Thorlabs PM122D) to measure the power of the incident light P_{inc} impinging on the synthetic aperture metalens through an array of pinholes with a size identical to the synthetic aperture. Subsequently, a pinhole of 100- μm -diameter is placed in front of the photodetector. We spatially scan the position of the photodetector near the designed focal point of the metalens and identify the maximum readout P_f . The focusing efficiency of the metalens η is then estimated as $\eta = P_f/P_{inc}$.

APPENDIX C: IMAGE RECOVERY PROCESS

The image recovery process consists of three steps: histogram stretching, Richardson–Lucy deconvolution, and median filtering. The histogram stretching step [68] is implemented first to improve the image contrast. The Richardson–Lucy deconvolution algorithm is an iterative method to recover an underlying image from a blurred image with a known PSF of the imaging system, by assuming a Poisson distribution of the noise [55,56].

Based on the Bayesian principle, the statistical model of the as-obtained image $g(x, y)$ and the target object $f(x, y)$ of an imaging system can be expressed as

$$p(f|g) = \frac{p(g|f)p(f)}{p(g)}. \tag{C1}$$

The goal of the Richardson–Lucy deconvolution algorithm is to maximize $p(f|g)$. While $p(g)$ and $p(f)$ can be considered as constant, the problem is then transformed to maximize $p(g|f)$, which is the probability of PSF $h(x, y)$. Based on the assumption that the noise in the image follows the Poisson statistical model, $p(g|f)$ can be expressed as

$$p(g|f) = \prod_{(x,y)} \frac{h(x,y) * f(x,y)^{g(x,y)} e^{-(h*f)(x,y)}}{g(x,y)!}. \tag{C2}$$

Finding the maximum value of $p(g|f)$ is equivalent to solving the iterative equation,

$$f^{(k+1)}(x,y) = \left[\frac{g(x,y)}{h(x,y) * f^{(k)}(x,y)} * h(x,y)^T \right] f^{(k)}(x,y), \tag{C3}$$

where $f^{(k)}(x, y)$ is the estimated object after k iterations. Subsequently, a final step of median filtering [68] is added to further reduce the noise of the recovered image. The effect of each step in the image recovery process is shown in Fig. 7.

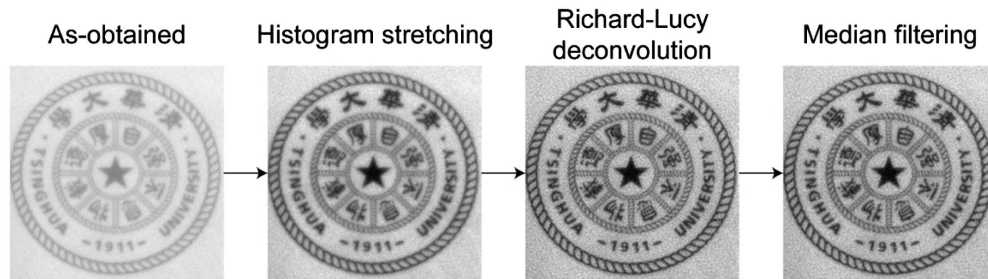


Fig. 7. Schematic of the image restoration process consisting of histogram stretching, Richardson–Lucy deconvolution, and median filtering.

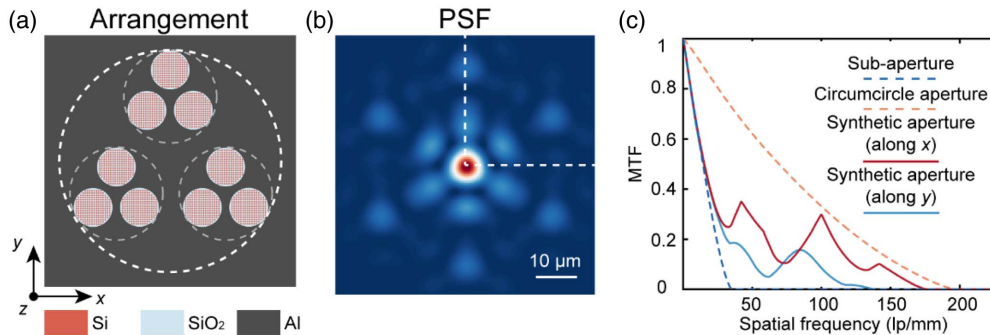


Fig. 8. Design of a nine-subaperture metalens. (a) Schematic of the arrangement of synthetic aperture metalens with nine subapertures. The white dashed line marks the circumcircle of the synthetic aperture. (b) Calculated PSF of the nine-subaperture synthetic aperture metalens; (c) calculated MTF of the nine-subaperture synthetic aperture metalens with comparison to the subaperture and circumcircle aperture cases.

APPENDIX D: SYNTHETIC APERTURE METALENS MADE OF MORE SUBAPERTURES

To further test the efficacy of the proposed method for scaling to an even larger aperture size, following the method proposed in the literature [52,69], we also designed a nine-subaperture metalens by using the arrangement of three-subaperture metalens three times. The diameter of the subaperture and circumference aperture are set to 0.84 mm and 4.76 mm, respectively, which leads to a fill factor of 0.28. $\lambda = 800$ nm is the design wavelength, and $f = 30$ mm is the focal length. Figure 8 shows a schematic of the arrangement of the nine-subaperture metalens along with the calculated PSF and MTF. The MCF of the MTF of the nine-subaperture metalens is greatly improved to a level comparable to the circumcircle aperture lens, similar to the MTF response of a synthetic aperture metalens with fewer subapertures.

Funding. National Natural Science Foundation of China (61975251).

Acknowledgment. This work was supported by the Center of High Performance Computing, Tsinghua University.

Disclosures. The authors declare no competing financial interest.

Data Availability. Data underlying the results presented in this paper are not publicly available at this time but may be obtained from the authors upon reasonable request.

REFERENCES

- P. Sandri, P. Mazzinghi, and V. Da Deppo, "Double Donut Schmidt Camera, a wide-field, large-aperture, and lightweight space telescope for the detection of ultrahigh energy cosmic rays," *Appl. Opt.* **57**, 3078–3087 (2018).
- L. Yuan, J. N. Xie, Z. He, Y. Wang, and J. Wang, "Optical design and evaluation of airborne prism-grating imaging spectrometer," *Opt. Express* **27**, 17686–17700 (2019).
- N. Yu and F. Capasso, "Flat optics with designer metasurfaces," *Nat. Mater.* **13**, 139–150 (2014).
- M. Khorasaninejad and F. Capasso, "Metalenses: versatile multifunctional photonic components," *Science* **358**, eaam8100 (2017).
- P. Lalanne and P. Chavel, "Metalenses at visible wavelengths: past, present, perspectives," *Laser Photon. Rev.* **11**, 1600295 (2017).
- P. Cheben, R. Halir, J. H. Schmid, H. A. Atwater, and D. R. Smith, "Subwavelength integrated photonics," *Nature* **560**, 565–572 (2018).
- M. L. Tseng, H.-H. Hsiao, C. H. Chu, M. K. Chen, G. Sun, A.-Q. Liu, and D. P. Tsai, "Metalenses: advances and applications," *Adv. Opt. Mater.* **6**, 1800554 (2018).
- S. M. Kamali, E. Arbabi, A. Arbabi, and A. Faraon, "A review of dielectric optical metasurfaces for wavefront control," *Nanophotonics* **7**, 1041–1068 (2018).
- J. Engelberg and U. Levy, "The advantages of metalenses over diffractive lenses," *Nat. Commun.* **11**, 1991 (2020).
- S.-W. Moon, Y. Kim, G. Yoon, and J. Rho, "Recent progress on ultrathin metalenses for flat optics," *iScience* **23**, 101877 (2020).
- H. Li, X. Xiao, B. Fang, S. Gao, Z. Wang, C. Chen, Y. Zhao, S. Zhu, and T. Li, "Bandpass-filter-integrated multiwavelength achromatic metalens," *Photon. Res.* **9**, 1384–1390 (2021).
- L. Huang, X. Chen, H. Mühlenbernd, H. Zhang, S. Chen, B. Bai, Q. Tan, G. Jin, K.-W. Cheah, C.-W. Qiu, J. Li, T. Zentgraf, and S. Zhang, "Three-dimensional optical holography using a plasmonic metasurface," *Nat. Commun.* **4**, 2808 (2013).
- Y. Yang, W. Wang, P. Moitra, Kravchenko II, D. P. Briggs, and J. Valentine, "Dielectric meta-reflectarray for broadband linear polarization conversion and optical vortex generation," *Nano Lett.* **14**, 1394–1399 (2014).
- A. Arbabi, Y. Horie, M. Bagheri, and A. Faraon, "Dielectric metasurfaces for complete control of phase and polarization with subwavelength spatial resolution and high transmission," *Nat. Nanotechnol.* **10**, 937–943 (2015).
- X. Ding, F. Monticone, K. Zhang, L. Zhang, D. Gao, S. N. Burokur, A. de Lustrac, Q. Wu, C. W. Qiu, and A. Alu, "Ultrathin Pancharatnam-Berry metasurface with maximal cross-polarization efficiency," *Adv. Mater.* **27**, 1195–1200 (2015).
- M. Khorasaninejad, W. T. Chen, R. C. Devlin, J. Oh, A. Y. Zhu, and F. Capasso, "Metalenses at visible wavelengths: diffraction-limited focusing and subwavelength resolution imaging," *Science* **352**, 1190–1194 (2016).
- Y. Zhou, Kravchenko II, H. Wang, J. R. Nolen, G. Gu, and J. Valentine, "Multilayer noninteracting dielectric metasurfaces for multiwavelength metaoptics," *Nano Lett.* **18**, 7529–7537 (2018).
- W. T. Chen, A. Y. Zhu, V. Sanjeev, M. Khorasaninejad, Z. J. Shi, E. Lee, and F. Capasso, "A broadband achromatic metalens for focusing and imaging in the visible," *Nat. Nanotechnol.* **13**, 220–226 (2018).
- H. Liang, Q. Lin, X. Xie, Q. Sun, Y. Wang, L. Zhou, L. Liu, X. Yu, J. Zhou, T. F. Krauss, and J. Li, "Ultrahigh numerical aperture metalens at visible wavelengths," *Nano Lett.* **18**, 4460–4466 (2018).
- G.-Y. Lee, G. Yoon, S.-Y. Lee, H. Yun, J. Cho, K. Lee, H. Kim, J. Rho, and B. Lee, "Complete amplitude and phase control of light using broadband holographic metasurfaces," *Nanoscale* **10**, 4237–4245 (2018).
- E. Arbabi, S. M. Kamali, A. Arbabi, and A. Faraon, "Full-Stokes imaging polarimetry using dielectric metasurfaces," *ACS Photon.* **5**, 3132–3140 (2018).
- R. Z. Zhao, B. Sain, Q. S. Wei, C. C. Tang, X. W. Li, T. Weiss, L. L. Huang, Y. T. Wang, and T. Zentgraf, "Multichannel vectorial holographic display and encryption," *Light Sci. Appl.* **7**, 95 (2018).
- N. A. Rubin, G. D'Aversa, P. Chevalier, Z. J. Shi, W. T. Chen, and F. Capasso, "Matrix Fourier optics enables a compact full-Stokes polarization camera," *Science* **365**, eaax1839 (2019).
- A. C. Overvig, S. Shrestha, S. C. Malek, M. Lu, A. Stein, C. Zheng, and N. Yu, "Dielectric metasurfaces for complete and independent control of the optical amplitude and phase," *Light Sci. Appl.* **8**, 92 (2019).
- C. Zhang, S. Divitt, Q. Fan, W. Zhu, A. Agrawal, Y. Lu, T. Xu, and H. J. Lezec, "Low-loss metasurface optics down to the deep ultraviolet region," *Light Sci. Appl.* **9**, 55 (2020).
- Y. Ni, S. Chen, Y. Wang, Q. Tan, S. Xiao, and Y. Yang, "Metasurface for structured light projection over 120 degrees field of view," *Nano Lett.* **20**, 6719–6724 (2020).
- R. Zhu, T. Qiu, J. Wang, S. Sui, C. Hao, T. Liu, Y. Li, M. Feng, A. Zhang, C. W. Qiu, and S. Qu, "Phase-to-pattern inverse design paradigm for fast realization of functional metasurfaces via transfer learning," *Nat. Commun.* **12**, 2974 (2021).
- S. Wang, Z. L. Deng, Y. Wang, Q. Zhou, X. Wang, Y. Cao, B. O. Guan, S. Xiao, and X. Li, "Arbitrary polarization conversion dichroism metasurfaces for all-in-one full Poincaré sphere polarizers," *Light Sci. Appl.* **10**, 24 (2021).
- F. Zhao, R. Lu, X. Chen, C. Jin, S. Chen, Z. Shen, C. Zhang, and Y. Yang, "Metalens-assisted system for underwater imaging," *Laser Photon. Rev.* **15**, 2100097 (2021).
- T. Badloe, I. Kim, Y. Kim, J. Kim, and J. Rho, "Electrically tunable bifocal metalens with diffraction-limited focusing and imaging at visible wavelengths," *Adv. Sci.* **2102646** (2021).
- C. Zhang, H. Subbaraman, Q. Li, Z. Pan, J. G. Ok, T. Ling, C.-J. Chung, X. Zhang, X. Lin, R. T. Chen, and L. J. Guo, "Printed photonic elements: nanoimprinting and beyond," *J. Mater. Chem. C* **4**, 5133–5153 (2016).
- J.-S. Park, S. Zhang, A. She, W. T. Chen, P. Lin, K. M. A. Yousef, J.-X. Cheng, and F. Capasso, "All-glass, large metalens at visible wavelength using deep-ultraviolet projection lithography," *Nano Lett.* **19**, 8673–8682 (2019).

33. G. Yoon, K. Kim, D. Huh, H. Lee, and J. Rho, "Single-step manufacturing of hierarchical dielectric metalens in the visible," *Nat. Commun.* **11**, 2268 (2020).
34. G. Yoon, K. Kim, S.-U. Kim, S. Han, H. Lee, and J. Rho, "Printable nanocomposite metalens for high-contrast near-infrared imaging," *ACS Nano* **15**, 698–706 (2021).
35. T. Hu, C.-K. Tseng, Y. H. Fu, Z. Xu, Y. Dong, S. Wang, K. H. Lai, V. Bliznetsov, S. Zhu, Q. Lin, and Y. Gu, "Demonstration of color display metasurfaces via immersion lithography on a 12-inch silicon wafer," *Opt. Express* **26**, 19548–19554 (2018).
36. A. She, S. Zhang, S. Shian, D. R. Clarke, and F. Capasso, "Large area metalenses: design, characterization, and mass manufacturing," *Opt. Express* **26**, 1573–1585 (2018).
37. S. Colburn, A. Zhan, and A. Majumdar, "Varifocal zoom imaging with large area focal length adjustable metalenses," *Optica* **5**, 825–831 (2018).
38. A. B. Meinel, "Aperture synthesis using independent telescopes," *Appl. Opt.* **9**, 2501–2504 (1970).
39. R. Barakat, "Dilute aperture diffraction imagery and object reconstruction," *Opt. Eng.* **29**, 131–139 (1990).
40. E. Sabatke and J. Burge, "Basic principles in the optical design of imaging multiple aperture systems," *Proc. SPIE* **4832**, 236–248 (2002).
41. Y. S. Jiang, J. J. Zhang, Y. T. He, H. Y. Wang, J. Wang, and J. Zhang, "Optical aperture synthesis imaging with fractional Fourier-domain filtering," *J. Opt. Soc. Am. A* **29**, 295–302 (2012).
42. T. Liu, J. Hu, L. Zhu, R. Zhou, C. Zhang, C. Wang, A. Zeng, and H. Huang, "Large effective aperture metalens based on optical sparse aperture system," *Chin. Opt. Lett.* **18**, 100001 (2020).
43. K. Akiyama, A. Alberdi, W. Alef, K. Asada, and R. Azulay, "First M87 event horizon telescope results. II. Array and instrumentation," *Astrophys. J. Lett.* **875**, L2 (2019).
44. S. Chung, D. W. Miller, and O. L. De Weck, "ARGOS testbed: study of multidisciplinary challenges of future spaceborne interferometric arrays," *Opt. Eng.* **43**, 2156–2167 (2004).
45. J. Turner, H. Estrada, M. Kneipp, and D. Razansky, "Universal weighted synthetic aperture focusing technique (W-SAFT) for scanning optoacoustic microscopy," *Optica* **4**, 770–778 (2017).
46. S. Colburn, A. Zhan, and A. Majumdar, "Metasurface optics for full-color computational imaging," *Sci. Adv.* **4**, eaar2114 (2018).
47. L. Huang, J. Whitehead, S. Colburn, and A. Majumdar, "Design and analysis of extended depth of focus metalenses for achromatic computational imaging," *Photon. Res.* **8**, 1613–1623 (2020).
48. S. Tan, F. Yang, V. Boominathan, A. Veeraraghavan, and G. V. Naik, "3D imaging using extreme dispersion in optical metasurfaces," *ACS Photon.* **8**, 1421–1429 (2021).
49. R. F. James, K. G. Douglas, L. Harrington, A. M. Kowalczyk, J. M. Jason, and A. M. James, "Comparison of reconstruction algorithms for images from sparse-aperture systems," *Proc. SPIE* **4792**, 1–8 (2002).
50. D. Wang, "Experimental study on imaging and image restoration of optical sparse aperture systems," *Opt. Eng.* **46**, 103201 (2007).
51. Y. Wu, M. Hui, W. Li, M. Liu, L. Dong, L. Kong, and Y. Zhao, "MTF improvement for optical synthetic aperture system via mid-frequency compensation," *Opt. Express* **29**, 10249–10264 (2021).
52. M. J. E. Golay, "Point arrays having compact, nonredundant autocorrelations," *J. Opt. Soc. Am.* **61**, 272–273 (1971).
53. N. J. Miller, M. P. Dierking, and B. D. Duncan, "Optical sparse aperture imaging," *Appl. Opt.* **46**, 5933–5943 (2007).
54. K. Matsushima and T. Shimobaba, "Band-limited angular spectrum method for numerical simulation of free-space propagation in far and near fields," *Opt. Express* **17**, 19662–19673 (2009).
55. W. Richardson, "Bayesian-based iterative method of image restoration," *J. Opt. Soc. Am.* **62**, 55–59 (1972).
56. L. Lucy, "An iterative technique for the rectification of observed distributions," *Astron. J.* **79**, 745 (1974).
57. A. Horé and D. Ziou, "Image quality metrics: PSNR vs. SSIM," in *20th International Conference on Pattern Recognition* (2010), pp. 2366–2369.
58. H. Chen, Z. Cen, C. Wang, S. Lan, and X. Li, "Image restoration via improved Wiener filter applied to optical sparse aperture systems," *Optik* **147**, 350–359 (2017).
59. M. Hui, Y. Wu, W. Li, M. Liu, L. Dong, L. Kong, and Y. Zhao, "Image restoration for synthetic aperture systems with a non-blind deconvolution algorithm via a deep convolutional neural network," *Opt. Express* **28**, 9929–9943 (2020).
60. J. Tang, K. Wang, Z. Ren, W. Zhang, X. Wu, J. Di, G. Liu, and J. Zhao, "RestoreNet: a deep learning framework for image restoration in optical synthetic aperture imaging system," *Opt. Laser Eng.* **139**, 106463 (2021).
61. J. Engelberg and U. Levy, "Achromatic flat lens performance limits," *Optica* **8**, 834–845 (2021).
62. J. P. Balthasar Mueller, N. A. Rubin, R. C. Devlin, B. Groever, and F. Capasso, "Metasurface polarization optics: independent phase control of arbitrary orthogonal states of polarization," *Phys. Rev. Lett.* **118**, 113901 (2017).
63. S. M. Wang, P. C. Wu, V. C. Su, Y. C. Lai, M. K. Chen, H. Y. Kuo, B. H. Chen, Y. H. Chen, T. T. Huang, J. H. Wang, R. M. Lin, C. H. Kuan, T. Li, Z. L. Wang, S. N. Zhu, and D. P. Tsai, "A broadband achromatic metalens in the visible," *Nat. Nanotechnol.* **13**, 227–232 (2018).
64. S. Colburn and A. Majumdar, "Metasurface generation of paired accelerating and rotating optical beams for passive ranging and scene reconstruction," *ACS Photon.* **7**, 1529–1536 (2020).
65. E. Tseng, S. Colburn, J. Whitehead, L. Huang, S.-H. Baek, A. Majumdar, and F. Heide, "Neural nano-optics for high-quality thin lens imaging," arXiv:2102.11579 (2021).
66. W. Liu, D. Ma, Z. Li, H. Cheng, D.-Y. Choi, J. Tian, and S. Chen, "Aberration-corrected three-dimensional positioning with a single-shot metalens array," *Optica* **7**, 1706–1713 (2020).
67. I. Kim, R. J. Martins, J. Jang, T. Badloe, S. Khadir, H.-Y. Jung, H. Kim, J. Kim, P. Genevet, and J. Rho, "Nanophotonics for light detection and ranging technology," *Nat. Nanotechnol.* **16**, 508–524 (2021).
68. R. C. Gonzalez and R. E. Woods, *Digital Image Processing* (Publishing House of Electronics Industry, 2020).
69. L. Qian, Q. Wu, F. Wu, and W. Shen, "Study on imaging of dual three sub-apertures design," *Acta Opt. Sin.* **25**, 1030–1035 (2005).